HHS Public Access

Author manuscript

J Chem Inf Model. Author manuscript; available in PMC 2022 November 22.

Published in final edited form as:

J Chem Inf Model. 2021 November 22; 61(11): 5614–5625. doi:10.1021/acs.jcim.1c00879.

Structural Insights into the Human Mitochondrial Pyruvate Carrier Complexes

Liang Xu[†], **Clyde F. Phelix**[#], **Liao Y. Chen**[†]

[†]Department of Physics and Astronomy, The University of Texas at San Antonio, One UTSA Circle, San Antonio, TX, 78249, USA.

[#]Department of Integrative Biology, The University of Texas at San Antonio, One UTSA Circle, San Antonio, TX, 78249, USA

Abstract

Pyruvate metabolism requires the mitochondrial pyruvate carrier (MPC) proteins to transport pyruvate from the intermembrane space through the inner mitochondrial membrane to the mitochondrial matrix. The lack of the atomic structures of MPC hampers the understanding of the functional states of MPC and molecular interactions with substrate or inhibitor. Here we develop the *de novo* models of human MPC complexes and characterize the conformational dynamics of the MPC heterodimer formed by MPC1 and MPC2 (MPC1/2) by computational simulations. Our results reveal that functional MPC1/2 prefers to adopt an inward-open conformation, with the carrier open to the matrix side, whereas the outward-open states are less populated. The energy barrier for pyruvate transport in MPC1/2 is low enough, and the inhibitor UK5099 blocks the pyruvate transport by stably binding to MPC1/2. Notably, consistent with experimental results, the MPC1 L79H mutation significantly alters the conformations of the MPC1/2 and thus fails for substrate transport. However, the MPC1 R97W mutation seems to retain the transport activity. The present *de novo* models of MPC complexes provide structural insights into the conformational states of MPC complexes and mechanistic understanding of interactions between substrate/inhibitor and MPC proteins.

Graphical Abstract

Corresponding author: liang.xu@utsa.edu.

Supporting Information

Summary of the simulations (including replica simulations) performed in this work (Table S1–Table S3); Comparison of structural models predicted by RoseTTAFold and AlphaFold (Fig. S1); The RESP partial charges for pyruvate, pyruvic acid, and UK5099 molecule (Fig. S2); The fraction of native contact Q and root-mean-square deviations (RMSDs) calculated for different MPC dimers (Fig. S3); Interaction energies calculated between MPC1 and MPC2 in different MPC1 complexes (Fig. S4); A representative conformation of MPC1/2 heterodimer in an outward-open state (Fig. S5); Effects on the N-terminal dynamics on the conformational states (Fig. S6); Results of MD simulations of MPC1/2 in complex with pyruvates (Fig. S7); Results of MD simulations of MPC1/2 in complex with pyruvic acids (Fig. S8); Repeated simulations of MPC1/2 in complex with UK5099 (Fig. S9); Contact maps calculated for MPC1/2 heterodimer carrying MPC1 L79H and R97W mutations (Fig. S10 and Fig. S11); Replica simulations of MPC1/2 heterodimer with the MPC1 L79H mutation (Fig. S12–Fig. S14); Replica simulations of MPC1/2 heterodimer with the MPC1 R97W mutation (Fig. S15–Fig. S18); Contacting residues between MPC1 and MPC2 in MPC1/2 heterodimer (Table S4), MPC1 homodimer (Table S5) and MPC2 homodimer (Table S6).

The authors declare no competing financial interest.

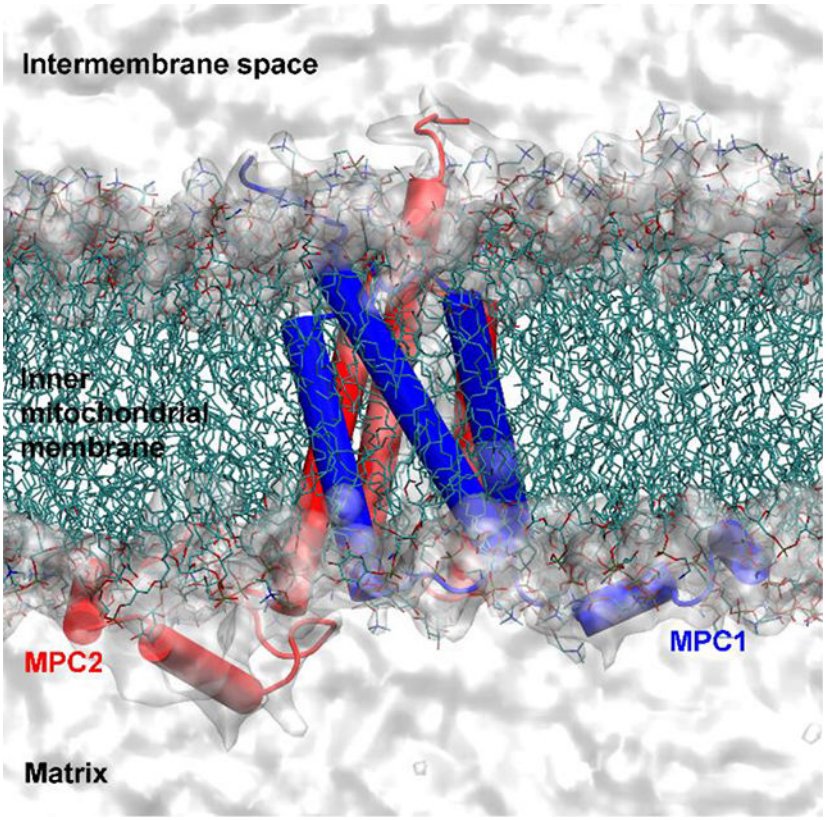

Introduction

The mitochondrial pyruvate carrier (MPC) proteins in the inner mitochondrial membrane (IMM) facilitate the metabolism of pyruvate by contributing the final step of pyruvate transport from the cytoplasm into the mitochondrial matrix.[1–3] Aberrant pyruvate metabolism due to dysfunctional MPC has been associated with cancer, heart failure, and neurodegeneration.[3–5] MPC proteins have been identified in humans, yeast, *Drosophila*, as well as in plants.[2, 6] In humans, two molecular identities of the MPC have been identified, *i.e.,* MPC1 (12 kD) and MPC2 (14 kD), which are composed of 109 and 127 amino acids respectively.[7, 8] In yeast, three MPC proteins were identified, including MPC1, MPC2, and MPC3, which are composed of 130, 129, and 146 amino acids, respectively. The sequence identity between human and yeast MPCs varies from 40% to 49%. The functional states of human MPCs have been proposed as ~150-kD oligomers formed by MPC1 and MPC2.[7, 8] However, such complexes could contain lipid/detergent micelle also, suggesting the presence of even lower molecular weight MPC complexes.[2] In yeast, the functional states of MPC have been identified as heterodimers formed by either MPC1 and MPC2 (MPC1/2) or MPC1 and MPC3 (MPC1/3).[9, 10] The human MPC homo- and heterodimers have also been reported recently, showing that the MPC heterodimers appear more stable and exist as the main functional state in support of pyruvate metabolism.[11]

Since no crystal structures of MPC proteins are available to date, investigation of the structure-function relationship of MPC proteins remains a large challenge.[12] Previous

experimental data suggested that yeast MPC1 may have only two transmembrane helices, but MPC2 and MPC3 may contain three transmembrane helices.[9] As a result, the yeast MPC1/2 and MPC1/3 heterodimers would use five transmembrane helices to form a functional pyruvate transport path in yeast, which seems not feasible because no other transmembrane transporters in the solute carrier family (SLC) (MPC defines a unique SLC family: SLC54A) involve only five transmembrane helices.[12] The smallest carrier in the SLC50 family, *i.e.*, the bacterial SemiSWEET glucose transporters, whose functional unit is the homodimer of the SemiSWEET protein, has six transmembrane helices in total.[13, 14] In addition, other experimental evidence suggests that the yeast MPC1 may possess three transmembrane helices like MPC2 and MPC3.[15] Because the monomeric SemiSWEET protein (~100 residues) includes three transmembrane helices and an N-terminal amphipathic helix and thus resembles the topology proposed for yeast MPC2 and MPC3, the SemiSWEET protein has been used as a template for homology modelling of the MPC complexes.[2, 11] However, because the sequence identity between the MPC and SemiSWEET protein is only ~10%,[12], a careful evaluation of the homology models of MPC based on the SemiSWEET protein seems necessary. Also, Phelix and coworkers have previously reported on a homology model of human and plant MPC1/2 heterodimer, using RaptorX and PyDock with respiratory complex I from *E. coli*, (PDB ID: 3RKO) as the template.[6, 16] Alternative template-free methods of protein modeling, *de novo* protein prediction, are using deep learning, such as the methods implemented in Rosetta,[17, 18] These methods have been successfully applied to predict different types of protein structures including membrane proteins.[19–21]

During substrate translocation, the SemiSWEET may adopt different conformational states including the outward-open and the inward-open conformations in which the substrate may alternatively access the extracellular and intracellular spaces.[14, 22, 23] In contrast, the conformational states of MPC proteins remain unclear due to the lack of reliable structural models. In this work, we proposed *de novo* models of MPC complexes, and fully relaxed these structures in a lipid bilayer of IMM by performing molecular dynamics (MD) simulations. The resulting MPC1/2 heterodimer has six transmembrane helices and favors an inward-open conformation (opening to the matrix side). Furthermore, our results provide structural insights into the molecular mechanism of the inhibitor UK5099 and the distinct effects of two MPC1 mutations (L79H and R97W) on the conformational dynamics of MPC1/2 heterodimer.

Methods

De novo modeling of human MPC complexes

We focused on the sequences of human MPC1 (UniProt ID: Q9Y5U8) and MPC2 (UnitProt ID: O95563). The deep learning based modeling method, TrRosetta, which is available for protein prediction on Robetta web server (https://robetta.bakerlab.org/),[24] was applied to predict a 3D structural model of MPC1 and MPC2 monomers first.[25] The only input for this web server is the MPC amino acid sequence. The output models were found to display a similar topology and further ranked according to the Rosetta energy function.[26] Because the Robetta server accepts only one sequence, to predict the structure of MPC homo- or

heterodimer, a linker containing 20/30 alanine/glycine residues were inserted between two MPC1, two MPC2, and MPC1 and MPC2 (starting from either MPC1 or MPC2) sequences. The predicted models were also ranked in terms of the Rosetta energy function, and the model with the lowest energy was selected for respective MPC dimer. Three dimers, MPC1 and MPC2 homodimers, and one MPC1/2 heterodimer, were found to display a similar fold. Of interest, the MPC monomer in each dimer was nearly identical with the predicted MPC monomer. Such results seemed expected as the monomeric sequence of MPC had become the training sequence that was used to predict the monomer structure in the MPC dimers. The *de novo* model of MPC1/2 dimer is shown in Fig. 1. The predicted MPC dimer with the linker is compactly arranged, especially the parallel arrangement of MPC1 and MPC2. Since the N-terminal amphipathic helix of MPC1 and MPC2 folded around the TM helices, we manually repositioned this segment in both MPC1 and MPC2 to be parallel with the membrane surface. The final MPC1/2 heterodimer was obtained after removing the linker (Fig. 1C). Applying the same procedure, the *de novo* models of MPC1 and MPC2 homodimers were also obtained. Note that all MPC dimers adopted a similar topology with the dimeric form of the SemiSWEET protein (Fig. 1D).

Recently the above Robetta web server changed its default method from TrRosetta to RoseTTAFold,[27] we have then compared the structural models predicted by the new RoseTTAFold approach with those models discussed in the current work. Nearly identical structural models were obtained. In addition to the above methods, an alternative deep learning algorithm, AlphaFold,[28] has also been developed for protein structural prediction. To compare the current models with those predicted by AlphaFold, the AlphaFold (v 2.0.0) installed at Frontera, a supercomputing cluster at Texas Advanced Computing Center, was applied to predict the structural models of MPC1, MPC2, and MPC1/2 heterodimer. Results were summarized in Fig. S1. Note that the structural models yielded by AlphaFold displayed a similar fold and overlapped well with the current MPC models, providing additional support for the MPC models discussed in the present work.

MD simulations of MPC complexes in inner mitochondria membrane

In current MD simulations, the IMM was modeled as an asymmetric lipid bilayer including the outer layer and inner layer. The composition of each layer was taken from the simulation study of the mitochondrial membranes:[29] the outer monolayer of IMM contains 50% POPC, 40% POPE, and 10% CRDL; whereas, the inner monolayer contains 30% POPC, 30% POPE, 30% CRDL, and 10% SAPI. Note that the outer and inner monolayer face to the intermembrane space (IMS) and matrix side, respectively (Fig. 1C). And the inner monolayer contains more negatively charged lipids (CRDL and SAPI lipids).

MD simulations of MPC1 and MPC2 monomer in IMM were first performed to relax the MPC proteins. The CHARMM-GUI webserver (https://www.charmm-gui.org/) was used to generate the input files used for MD simulations.[30–33] The protein was solvated by adding a 25 Å thick water layer (TIP3P water molecules) below and above the lipid bilayer. The salt concentration (NaCl) in each system was 0.15 M. The protein and lipid structures were represented with the CHARMM36m and CHARMM36 force field parameters, respectively.[34, 35] The equilibration procedures were the same as used in

our previous studies of membrane proteins.[36, 37] Briefly, each system was first energy minimized for 10,000 steps, followed by six stages of equilibration with the harmonic constraints exerted on lipid, and protein heavy atoms. The force constants for lipid head group were decreased from 1000 kJ/(mol·nm^2) to 0, whereas the force constants for protein backbone and sidechain (denoted as backbone/sidechain) were gradually decreased from 4000/2000 kJ/(mol·nm^2) and 50/0 kJ/(mol·nm^2) during the equilibration procedures. The temperature was kept constant at 310 K using the Berendsen thermostat with a coupling parameter of 0.1 ps,[38] and the pressure was controlled at 1.0 bar using the Berendsen barostat with a time constant of 5.0 ps for the last four stages of equilibration.[38] The semiisotropic pressure coupling was applied for membrane simulations. A cutoff of 12 Å was applied for the van der Waals interactions and the long-range electrostatic interactions were treated using the particle mesh Ewald method.[39] The integration time step was 2 fs and trajectory was saved every 10 ps. The production dynamics were performed at constant temperature (310 K) controlled by the Nosé-Hoover thermostat[40, 41] and constant pressure (1.0 bar) controlled by the Parrinello-Rahman[42, 43] barostat without any restraints. All MD simulations were carried out using GROMACS simulation package (version 2019.6).[44–46]

After short (50–100 ns) relaxation, the electrostatic potential energy surface was calculated for MPC monomers and dimers using the Adaptive Poisson-Boltzmann Solver (APBS)[47] (Fig. 2). The N-terminal amphipathic helix of MPC1 and MPC2 was found to possess more positively charged surface, complementary to the negatively charged inner monolayer of IMM (matrix side). Thus, MPC1 and MPC2 tend to anchor to the IMM with the N-terminal amphipathic helix due to the electrostatic attraction. Such an orientation may further facilitate the formation of MPC dimer in a parallel arrangement.

MD simulations of MPC1/2 in complex with pyruvates and UK5099

To model the structure of MPC1/2 heterodimer in complex with pyruvate and the inhibitor UK5099,[48, 49] one conformation of MPC1/2 was randomly selected from the last 1.5-μs simulations of MPC1/2, and AutoDock Vina program[50] was applied to dock one pyruvate or UK5099 molecule into the MPC1/2 heterodimer. In the docking process, the MPC1/2 structure was modeled as rigid while the ligand structure was modeled as flexible. The optimal binding pose with the lowest binding energy was obtained. The protein structure was represented with the CHARMM36m force field parameters,[34] and the ligand structure was represented with the CHARMM General Force Field (CGenFF)[51] along with the RESP partial charges[52] (Fig. S2). To enhance sampling, four pyruvate molecules were placed in different sites of MPC1/2 at distances that would prevent them from influencing each other directly. MD simulations of MPC1/2 in complex with pyruvates or UK5099 were carried out under the same simulation conditions as described above. The pyruvate transport has been suggested to be highly dependent on the pH and coupled with H^+.[53] Different pH values in the intermembrane space and mitochondrial matrix have also been reported.[54, 55] Since no pH gradient was present in the current simulations, for comparison, MPC1/2 in complex with four pyruvic acids were also simulated with each pyruvic acid bound to the same site of MPC1/2 as occupied by each pyruvate molecule. All systems simulated in this work, including repeated simulations, are summarized in Tables S1–S3.

Results and Discussion

Structural characterization of human MPC1/2 heterodimer.

Fig. 1A shows that like SemiSWEET protein, the *de novo* models of MPC1 and MPC2 have three transmembrane helices. For additional comparison, homology modelling using the Modeller (v9.23) program was performed.[56] Fig. 1B shows the homology models of MPC1 and MPC2 using the SemiSWEET protein as the unique template. Besides the structural similarity between the *de novo* and homology models, the transmembrane helices involve distinct segments. Specifically, in the SemiSWEET protein (PDB ID: 4QND), the TM1 includes residues 19–31, TM2 includes residues 54–71, and TM3 includes residues 80–95. By contrast, in the *de novo* model of MPC1, TM1 includes residues 25–46, TM2 includes residues 53–73, and TM3 includes residues 77–107. In MPC2, TM1 includes residues 38–62, TM2 includes residues 68–89, and TM3 includes residues 94–126. To compare the relative stability of MPC monomers generated from different protocols, the Rosetta energy function was applied to calculate the conformational energy for each model.[26] The *de novo* model of MPC1 and MPC2 have a conformational energy of −358.5 (in Rosetta Energy Units, REU) and −430.8 (REU), respectively. However, the energy values are 26.6 (REU) and 10.0 (REU) for the homology models of MPC1 and MPC2, respectively. Hence, these homology models with SemiSWEET as the template seemed unfavorable, and we focused on the *de novo* models in the following sections.

Fig. 1C shows the most stable *de novo* model of MPC1/2 heterodimer screened in terms of the Rosetta energy function, in which the MPC1 and MPC2 were in a parallel orientation, and the N-terminal amphipathic helix was positioned to be parallel to the membrane surface. Because the N-terminal amphipathic helix is positively charged (Fig. 2), complementary to the negatively charged inner layer of IMM (matrix side), the N-terminal of MPC complex seems favorable to associate with the mitochondria matrix and the C-terminal resides within the intermembrane space (IMS) (Fig. 1C). Of note, such an orientation was also indicated for yeast MPC.[9, 10, 15] Fig. 1D shows the structural superposition of the *de novo* MPC dimers with the dimeric assembly of SemiSWEET protein, suggesting that MPC2 dimer shares a similar topology with the SemiSWEET homodimer and thus may also form a transporter with six transmembrane helices, consistent with a previous report.[57]

The three MPC dimers were individually relaxed in an asymmetric IMM by performing 3-μs MD simulations. The calculated fraction of native contact indicated that no significant fluctuations in the intramolecular contacts were observed after 1.5-μs simulations (Fig. S3). However, the backbone root-mean-square deviations of the transmembrane helices suggested that MPC1/2 heterodimer seemed more stable than MPC1 and MPC2 homodimers (Fig. S3). The calculated contact maps shown in Fig. 3 further demonstrate that there were more contacts between two MPC monomers in MPC1/2 that contribute to its stability. In MPC1/2 heterodimer, there were 49 contacts with contact frequencies greater than 50%, compared to the 34 contacts identified in MPC1 homodimer and 17 contacts identified in MPC2 homodimer. Moreover, the calculated interaction energies showed that there were more strong interactions between two MPC monomers in MPC1/2 heterodimer than in MPC1 and MPC2 homodimers (Fig. S4). Taken together, the above results collectively suggested that

the heterodimer formed by MPC1 and MPC2 appeared more stable than the homodimers formed by either MPC1 or MPC2, in agreement with a recent experimental study.[11]

To further characterize the conformational dynamics of MPC1/2 heterodimer, several distances of paired residues between MPC1 and MPC2 were calculated to determine the conformational states sampled by MPC1/2 (Fig. 4A). The distance between Pro48 of MPC1 and Pro63 of MPC2 was used to assess the open or close of the outward-facing side of MPC1/2; whereas the distance between Pro75 of MPC1 and Pro91 of MPC2 was used to assess the open or close of the inward-facing side of MPC1/2 (Fig. 4B). When the minimal distance between Asp43 of MPC1 and Arg62 of MPC2 was < 3.0 Å, a salt-bridge between the two residues would be expected (Fig. 4C). The remaining distance is between two bulky hydrophobic residues, Tyr62 of MPC1 and Trp82 of MPC2, which could act as the gating residues to define the open or close of the central path in MPC1/2 (Fig. 4D). The average distance between Pro48 of MPC1 and Pro68 of MPC2 (block averaged over the last 1.5-μs simulations) was 13.0 ± 0.2 Å, and the average distance between Pro75 of MPC1 and Pro91 of MPC2 was 22.0 ± 0.5 Å, indicating a wider opening of the inward-facing side of MPC1/2 (Fig. 4B). Moreover, the residues Asp43 of MPC1 and Arg62 of MPC2 had a high probability (73%) of participating in a salt-bridge (Fig. 4C), which may help to stabilize and narrow the outward-facing side of MPC1/2. In addition, the average distance between Tyr62 of MPC1 and Trp82 of MPC2 was 6.2 ± 0.3 Å, implying an open pathway in MPC1/2 (Fig. 4D). Taken together, the present simulations suggested that MPC1/2 heterodimer predominantly populated an inward-open state. Such a representative inward-open conformation was shown in Fig. 4A. The HOLE program was used[58] to determine the radius of the transport pathway. The minimal radius of 0.7 Å found in the transport pathway was at the same position where the salt-bridge between Asp43 of MPC1 and Arg62 of MPC2 was established. In addition to the inward-open state, the fluctuations in the different distances also suggested the presence of other less populated states and the possibility of state-to-state transition over MD simulations of MPC1/2 heterodimer. Fig. S5 shows a representative conformation of MPC1/2 in an outward-open state. In this outward-open conformation, no salt-bridge was formed between Asp43 of MPC1 and Arg62 of MPC2. The two gating residues, Tyr62 of MPC1 and Trp82 of MPC2, approached each other and blocked the transport pathway, resulting in the minimal radius of 0.03 Å at the same position of the passage (Fig. S5).

Since the N-terminal amphipathic helix is flexible relative to the transmembrane domain, and could adopt different orientations (Fig. S1), the effects of the N-terminal dynamics on the conformational states of MPC1/2 heterodimer were investigated. Three snapshots taken at t = 0, 1000 ns, and 3000 ns of the simulation were superimposed and their corresponding conformational states were compared. Interestingly, the dynamics of the N-terminal seemed to be restrained (Fig. S6). For instance, the N-terminal at the end of the simulation (t = 3000 ns) was in a position between the orientations at the starting (t = 0) and during the simulation (t = 1000 ns). However, the MPC1/2 heterodimer adopted an outward-open state at the t = 0, an inward-open state at t = 1000 ns, and an inward-open state at t = 3000 ns (Fig. 4), respectively. The above results indicate that the dynamics of the N-terminal may have little effect on the conformational states of MPC1/2 heterodimer over current simulations.

Characterization of pyruvate transport in MPC1/2 and inhibitory mechanism of UK5099.

Without crystal structures of MPC, how the well-established inhibitor UK5099 blocks pyruvate transport remains largely unclear. To examine the interactions of pyruvate with MPC1/2 heterodimer, four pyruvate molecules were simultaneously placed to the different binding sites of MPC1/2 as predicted by docking. In this way, we could enhance sampling of pyruvate transport in one simulation, and investigate the effect of the presence of a second pyruvate on the pyruvate transport. For the UK5099-bound MPC1/2 complex, one UK5099 was placed to the most favorable binding site of MPC1/2 as obtained by docking. MD simulations showed that one pyruvate (circled in yellow in Fig. 5A) moved toward the matrix side and left the MPC1/2 transport pathway at ~10 ns. Two pyruvate molecules with their initial positions above this pyruvate diffused into the IMS even faster; whereas the remaining pyruvate with its initial position below the circled one also diffused faster but into the matrix side. The contacting residues and corresponding frequencies during pyruvate transport are shown in Fig. 5B and Fig. 5C, respectively. Results of MD simulations of pyruvate-bound MPC1/2 initially in a different inward-open conformation are shown in Fig. S7, and results of MD simulations of MPC1/2 in complex with pyruvic acids are shown in Fig. S8. Since the time scale for pyruvate/pyruvic acid transport varied from 4 ns to 236 ns, we focused on the relative values of the contact frequency and identified those MPC1/2 residues involving in the substrate transport. Combining all results from simulations of MPC1/2 in complex with pyruvate/pyruvic acid (Fig. 5, Fig. S7, and Fig. S8), Asn33, Leu36, His84, and Asn87 in MPC1, and Leu52, Ala55, Leu75, Trp82, Asn100, and Val103 in MPC2 appeared as important interfering residues that may define the transport pathway of substrates in MPC1/2 heterodimer (Fig. 5B). The above results also revealed that the energy barriers for substrate transport were rather low, independent of the conformational states of MPC1/2 heterodimer. And the presence of additional pyruvate may not affect the transport of pyruvate in the MPC1/2 heterodimer in these simulations. Of interest, the glucose transport in the SemiSWEET was also observed to resemble a “free ride”, with SemiSWEET adopting the same conformation.[22]

Fig. 6 summarizes the results of simulations of MPC1/2 in complex with UK5099. The initial binding site of UK5099 was predicted by molecular docking (Fig. 6A). The distance between the center-of-mass of MPC1/2 and the center-of-mass of UK5099 implied that UK5099 was trapped in the transport pathway of MPC1/2 over the 500-ns simulations (Fig. 6B). Moreover, UK5099 interacted with Leu36 and Asn87 of MPC1, and Leu52, Ala55, Leu75, Thr78, Gly79, Trp82, Asn100, and Val103 of MPC2, with contact frequencies >50% (Fig. 6C–6F). Similar results were also obtained from another independent simulation of MPC1/2 in complex with UK5099 (Fig. S9). Note that these interacting residues were also identified as interacting residues with pyruvate (Fig. 5), suggesting that UK5099 may inhibit the pyruvate transport by stably occupying the essential binding sites of pyruvate in MPC1/2.

Effects of L79H and R97W mutations in MPC1 on the conformational dynamics of MPC1/2 heterodimer.

Two pathogenic mutations, L79H and R97W in MPC1, have been described in patients, showing distinct effects on the formation and function of MPC1/2 complex.[59] The MPC1

L79H mutant could form stable complexes with MPC2, but the MPC1/2 complexes lost the function of pyruvate transport, *ex vivo* and *in vitro*. Conversely, the MPC1/2 complexes formed by MPC1 R97W mutant and MPC2, *ex vivo* and *in vitro,* retained the pyruvate transport function.[59] To investigate the effects of these two mutations on the conformational dynamics of MPC1/2 heterodimer, two independent simulations of MPC1/2 carrying the MPC1 L79H mutation were carried out, with one simulation starting from the inward-open conformation of MPC1/2 (Fig. 4A) and the other simulation starting from the outward-open conformation of MPC1/2 (Fig. S5). In each conformation of MPC1/2, the Leu79 or Arg97 of MPC1 was replaced by the residue His or Trp, respectively, and simulations including the minimization and equilibration were under the same conditions. The relative stability of MPC1/2 heterodimer containing MPC1 L79H mutation ($MPC1^{L79H}/2$) was assessed in terms of the contact maps (Fig. S10). Our results implied that the $MPC1^{L79H}/2$ heterodimer starting from the inward-open state was less stable than the corresponding $MPC1^{L79H}/2$ heterodimer starting from the outward-open conformation. Specifically, there were 48 pairs of contacting residues with contact frequencies > 50% in the $MPC1^{L79H}/2$ with the initial outward-open conformation, however, there were only 30 pair of contacting residues with frequencies > 50% in the $MPC1^{L79H}/2$ starting from the inward-open conformation (Fig. S10). The calculated interaction energies also indicated that $MPC1^{L79H}$ was more strongly associated with MPC2 in the $MPC1^{L79H}/2$ with the initial outward-open conformation (Table S2). We repeated the above two simulations, and found stronger interactions between $MPC1^{L79H}$ and MPC2 in $MPC1^{L79H}/2$ in both systems. The interaction energy for $MPC1^{L79H}/2$ with the initial outward-open state decreased from −128.8 kcal/mol to −142.4 kcal/mol, whereas the interaction energy for $MPC1^{L79H}/2$ with the initial inward-open state decreased from −49.4 kcal/mol to −116.7 kcal/mol (Table S2). The large fluctuation in the interaction energy of $MPC1^{L79H}/2$ with the initial inward-open state indicated that this conformation seemed more sensitive to the MPC1 L79H mutation, and may lead to significant conformational alterations. Taken together, the above results suggest that the $MPC1^{L79H}/2$ heterodimer with the initial outward-open conformation could be more stable and thus more populated.

The conformational dynamics of the most populated $MPC1^{L79H}/2$ heterodimer starting from the outward-open conformation were further characterized and results are shown in Fig. 7. Compared to the wild-type MPC1/2 (Fig. 4), the distance between Pro48 of MPC1 and Pro63 of MPC2 slightly decreased from 13.0 ± 0.2 Å to 12.2 ± 0.2 Å (block averaged over the last 500-ns trajectory). However, a significant decrease in the distance between Pro75 of MPC1 and Pro91 of MPC2 was observed (22.0 ± 0.5 Å *vs.* 16.2 ± 0.5 Å) in the $MPC1^{L79H}/2$ (Fig. 7B). Unlike the wild-type MPC1/2 (Fig. 4), no salt-bridge was formed between Asp43 of MPC1 and Arg62 of MPC2 (Fig. 7C), but the minimal distance between Tyr62 of MPC1 and Trp82 of MPC2 maintained at 2.3 ± 0.4 Å after 100-ns simulations (Fig. 7D). The above changes in the relevant distances suggested a narrower outward- facing and inward-facing side in $MPC1^{L79H}/2$ in which the pyruvate transport could actually be blocked due to the closure of the pathway at the position of the gating residues (Tyr62 of MPC1 and Trp82 of MPC2). Such a representative conformation of $MPC1^{L79H}/2$ was shown in Fig. 7A. In addition to the above distance restraints, the formation of short helices around Pro48 of MPC1 and Pro63 of MPC2 may also contribute to the minimal radius of

the transport pathway that occurred at the outward-facing side (Fig. 7A). Because of the narrowing in both sides of the transport pathway and the closure inside the pathway, this conformational state populated by MPC1^{L79H}/2 seemed different from the functional states (outward-open or inward-open state), and more like a dysfunctional form of MPC1/2 that failed to transport pyruvate. Note that this dysfunctional form of MPC1^{L79H}/2 was also observed in the repeated simulation (Fig. S12). The present results thus provided molecular insights into the mechanism of the dysfunction of MPC1/2 complexes caused by MPC1 L79H mutation.[59]

Similar to the simulations of MPC1^{L79H}/2, two independent simulations were also performed for MPC1/2 heterodimer carrying the MPC1 R97W mutation (MPC1^{R97W}/2). The relative stability of MPC1^{R97W}/2 was also assessed in terms of the contact maps (Fig. S11). There were 43 and 44 contacting residues for the MPC1^{R97W}/2 heterodimer starting from the outward-open and the inward-open conformations, respectively (Fig. S11). Similar to MPC1^{L79H}/2, interaction energies also suggest a stronger association between MPC1^{R97W} and MPC2 in the MPC1^{R97W}/2 starting from the outward-open state (Table. S3). Comparable interaction energies were obtained from repeated simulations, indicating that the MPC1^{R97W}/2 heterodimer may not be so sensitive to the MPC1 R97W mutation, and could populate different states originating from different initial conformations. The results of characterization of MPC1^{R97W}/2 starting from the inward-open and outward-open states of MPC1/2 are shown in Figs. S15–S18. Fig. S15 demonstrates that although Asp43 of MPC1 and Arg62 of MPC2 still have a probability of 38% to establish a salt-bridge, such a salt-bridge could not be stably established in the repeated simulation (Fig. S16). On the other hand, the inward-facing side of MPC1^{R97W}/2, especially the gating residues Tyr62 of MPC1 and Trp82 of MPC2, is widely open, corresponding to the inward-open states of MPC1/2. Also, Fig. S17 demonstrates that the distance between the two gating residues (Tyr62 of MPC1 and Trp82 of MPC2) can be < 3.0 Å (8%). And the outward-facing side (the distance between the Pro48 of MPC1 and Pro63 of MPC2) can be even wider than the inward-facing side (the distance between the Pro75 of MPC1 and Pro91 of MPC2). Such results indicate the possibility of sampling the outward-open state by MPC1^{R97W}/2. Since both outward-open and inward-open states could be accessed by MPC1^{R97W}/2 heterodimers, especially the substrate transport pathway is not blocked, it therefore seems reasonable to speculate that MPC1^{R97W}/2 could retain pyruvate transport activity, in line with the experimental reports.[59]

Conclusions

To bridge the gap between the structure and function of MPC proteins, *de novo* protein prediction was applied to develop the structural models of MPC complexes, which were further relaxed in a model of IMM by carrying out all-atom MD simulations. In particular, the conformational dynamics of the MPC1/2 complexes were characterized. Several conclusions emerged from the present simulation results when compared with available experimental data. First, the proposed *de novo* MPC models suggest the presence of three transmembrane helices and an N-terminal amphipathic helix in human MPC1 and MPC2 (Fig. 1). Although the general topology of the *de novo* MPC structures is similar to the SemiSWEET protein, the positions of transmembrane segments are different, and the *de*

novo models seem more stable than the homology models generated using the SemiSWEET protein as the template. Moreover, based on the electrostatic properties of MPC proteins and the IMM, MPC1 and MPC2 expose the N-terminus to the matrix side (Fig. 2), in line with the experimental evidence of the yeast MPC positions in IMM.[9, 10, 15] MPC1 and MPC2 adopt a parallel arrangement in both homo- and heterodimers, and the heterodimer appears to be more stable (Fig. 3).

Second, the conformational dynamics reveal that the MPC1/2 heterodimer favors an inward-open conformation, and the salt-bridge between Asp43 of MPC1 and Arg62 of MPC2 could stabilize such conformations (Fig. 4). Less populated states like the outward-open conformations were also visited by MPC1/2 heterodimer, indicating the feasibility of conformational transitions in the *de novo* MPC1/2 heterodimer. Third, depending on the initial conformations, the MPC1 L79H mutation in MPC1/2 heterodimer may populate distinct states, but the most populated and thus most stable states show a blocked pathway (Fig. 7), consistent with the dysfunctional effect of MPC1 L79H on pyruvate transport.[59] In contrast, the conformational states seem less sensitive to the MPC1 R97W mutation in MPC1/2, and therefore pyruvate transport activity can be retained, also consistent with the experimental results.[59] In addition to L79H and R97W mutations, our results also imply that Tyr62 of MPC1 and Trp82 of MPC2 are important to define the conformational states of MPC1/2, thus, mutations on the two residues may significantly alter the conformations of MPC1/2 and consequently affect the transport function of MPC complexes. Further investigations are required to gain molecular insights into the role of the two residues.

Finally, our results demonstrate that the inhibitor UK5099 could stably bind to the site that overlaps with the positions of interfering residues in the transport pathway of MPC1/2 over pyruvate translocation across the IMM. The pyruvate transport process is fast and unlikely to alter the conformations of MPC1/2, similar to the glucose transport in the SemiSWEET.[22] The present work provides valuable structural insights into the functional unit of MPC complexes. And the *de novo* models may be potentially useful for the design of novel inhibitors of MPC[60] and understanding of protein-ligand interactions.[61] However, the present work does not exclude the possibility of the presence of other pyruvate topology. The pyruvate inhibitor has been suggested to bind to the pyruvate site and react with the thiol (–SH) group.[53, 62] The present *de novo* structure of MPC1/2 does not show such interactions with residues containing a thiol-group. In contrast, in the proposed homology model of MPC1/2 heterodimer based on the template of the respiratory complex I from *E. coli*, (PDB ID: 3RKO), interactions of different substrates with -SH group within the carrier were possible.[6, 16] However, it should be noted that the rat mitochondria were used in the early experimental studies of MPC inhibitors.[60, 62] Although the sequence identity between rat MPC and human MPC proteins is > 90% (94.5% for MPC1 and 91.3% for MPC1), it remains largely unknown to what extent the difference in the sequence would lead to structural variation between rat and human MPC proteins. Moreover, in human, yeast, and *Drosophila*, MPC1 and MPC2 could be able to associate to form an ~150-kD complex in the inner mitochondrial membrane,[8] suggesting the formation of MPC oligomers larger than dimers. Thus, MPC inhibitors including UK5099 could be able to bind to the pocket formed in MPC oligomers and interact with a cysteine residue outside the pyruvate transport pathway. Results from the experimental study[60] seem also to support this assumption. In

that study, different source of rat mitochondria (heart, kidney, liver, and brain) displayed different concentrations of binding site (pmol per mg protein) for the same inhibitor, indicating the formation of various types of MPC oligomers with different ratios of rat MPC1 and MPC2. The presence of a hydrophobic binding site on the matrix surface of the carrier was indicated.[60] Taken together, UK5099 and other inhibitors may reversibly interact with cysteine resides of MPC when MPC proteins associate to form high-order oligomers, but could also block the pyruvate transport by directly binding to the inside of MPC1/2 heterodimer. The proposed hydrophobic binding sites for MPC inhibitors are most likely those binding pockets formed in MPC oligomers but not available in MPC1/2 heterodimers. Investigation of MPC oligomers appears interesting and challenging, and further studies are necessary to elucidate the structures and functions of the MPC proteins.

Supplementary Material

Refer to Web version on PubMed Central for supplementary material.

Acknowledgements

The authors acknowledge the Texas Advanced Computing Center (TACC) at The University of Texas at Austin for providing HPC resources that have contributed to the research results reported within this paper. URL: http://www.tacc.utexas.edu.

Funding

The authors acknowledge support from the NIH (Grant #GM121275).

Data and Software Availability:

For this study, Gromacs is available at https://www.gromacs.org; VMD is available at https://www.ks.uiuc.edu/Research/vmd/; Robetta sever is available at https://robetta.bakerlab.org/; Rosetta program is available at https://www.rosettacommons.org; AutoDock Vina is available at http://vina.scripps.edu; HOLE program is available at http://www.holeprogram.org; Modeller program is available at https://salilab.org/modeller; GNU plot is available at http://www.gnuplot.info. PDB structures are available from RCSB PDB (https://www.rcsb.org). The representative *de novo* models (in pdb format) are available with the manuscript. Scripts used for data analysis and other atomic structural models are available from the authors upon request.

References

1. McCommis Kyle S.; Finck Brian N. Mitochondrial pyruvate transport: a historical perspective and future research directions. Biochem. J 2015, 466, 443–454. [PubMed: 25748677]
2. Vanderperre B; Bender T; Kunji ERS; Martinou J-C Mitochondrial pyruvate import and its effects on homeostasis. Curr. Opin. Cell Biol 2015, 33, 35–41. [PubMed: 25463844]
3. Gray LR; Tompkins SC; Taylor EB Regulation of pyruvate metabolism and human disease. Cell. Mol. Life Sci 2013, 71, 2577–2604. [PubMed: 24363178]
4. Buchanan JL; Taylor EB Mitochondrial pyruvate carrier function in health and disease across the lifespan. Biomolecules 2020, 10, 1162.
5. Zangari J; Petrelli F; Maillot B; Martinou J-C The multifaceted pyruvate metabolism: role of the mitochondrial pyruvate carrier. Biomolecules 2020, 10, 1068.

6. Dugan JL; Bourdon AK; Phelix CF Mitochondrial pyruvate carrier 1 and 2 heterodimer, in silico, models of plant and human complexes. Int. J. Knowl. Discov. Bioinform 2017, 7, 11–42.
7. Herzig S; Raemy E; Montessuit S; Veuthey J-L; Zamboni N; Westermann B; Kunji ERS; Martinou J-C Identification and functional expression of the mitochondrial pyruvate carrier. Science 2012, 337, 93–96. [PubMed: 22628554]
8. Bricker DK; Taylor EB; Schell JC; Orsak T; Boutron A; Chen Y-C; Cox JE; Cardon CM; Van Vranken JG; Dephoure N; Redin C; Boudina S; Gygi SP; Brivet M; Thummel CS; Rutter J A mitochondrial pyruvate carrier required for pyruvate uptake in yeast, *Drosophila*, and humans. Science 2012, 337, 96–100. [PubMed: 22628558]
9. Bender T; Pena G; Martinou JC Regulation of mitochondrial pyruvate uptake by alternative pyruvate carrier complexes. EMBO J. 2015, 34, 911–924. [PubMed: 25672363]
10. Tavoulari S; Thangaratnarajah C; Mavridou V; Harbour ME; Martinou JC; Kunji ERS The yeast mitochondrial pyruvate carrier is a hetero-dimer in its functional state. EMBO J. 2019, 38, e100785. [PubMed: 30979775]
11. Lee J; Jin Z; Lee D; Yun J-H; Lee W Characteristic analysis of homo- and heterodimeric complexes of human mitochondrial pyruvate carrier related to metabolic diseases. Int. J. Mol. Sci 2020, 21, 3403.
12. Quesñay JEN; Pollock NL; Nagampalli RSK; Lee SC; Balakrishnan V; Dias SMG; Moraes I; Dafforn TR; Ambrosio ALB Insights on the quest for the structure–function relationship of the mitochondrial pyruvate carrier. Biology 2020, 9, 407.
13. Xu Y; Tao Y; Cheung LS; Fan C; Chen L-Q; Xu S; Perry K; Frommer WB; Feng L Structures of bacterial homologues of SWEET transporters in two distinct conformations. Nature 2014, 515, 448–452. [PubMed: 25186729]
14. Feng L; Frommer WB Structure and function of SemiSWEET and SWEET sugar transporters. Trends Biochem. Sci 2015, 40, 480–486. [PubMed: 26071195]
15. Rampelt H; Sucec I; Bersch B; Horten P; Perschil I; Martinou J-C; van der Laan M; Wiedemann N; Schanda P; Pfanner N The mitochondrial carrier pathway transports non-canonical substrates with an odd number of transmembrane segments. BMC Biology 2020, 18, 2. [PubMed: 31907035]
16. Phelix CF; Bourdon AK; Dugan JL; Villareal G; Perry G MSDC-0160 and MSDC-0602 binding with human mitochondrial pyruvate carrier (mpc) 1 and 2 heterodimer. Int. J. Knowl. Discov. Bioinform 2017, 7, 43–67.
17. Ovchinnikov S; Kim DE; Wang RY-R; Liu Y; DiMaio F; Baker D Improved de novo structure prediction in CASP11 by incorporating coevolution information into Rosetta. Proteins 2016, 84, 67–75. [PubMed: 26677056]
18. Kaufmann KW; Lemmon GH; DeLuca SL; Sheehan JH; Meiler J Practically useful: what the rosetta protein modeling suite can do for you. Biochemistry 2010, 49, 2987–2998. [PubMed: 20235548]
19. Hiranuma N; Park H; Baek M; Anishchenko I; Dauparas J; Baker D Improved protein structure refinement guided by deep learning based accuracy estimation. Nat. Commun 2021, 12, 1340. [PubMed: 33637700]
20. Vorobieva AA; White P; Liang B; Horne JE; Bera AK; Chow CM; Gerben S; Marx S; Kang A; Stiving AQ; Harvey SR; Marx DC; Khan GN; Fleming KG; Wysocki VH; Brockwell DJ; Tamm LK; Radford SE; Baker D *De novo* design of transmembrane β barrels. Science 2021, 371, eabc8182. [PubMed: 33602829]
21. Xu C; Lu P; Gamal El-Din TM; Pei XY; Johnson MC; Uyeda A; Bick MJ; Xu Q; Jiang D; Bai H; Reggiano G; Hsia Y; Brunette TJ; Dou J; Ma D; Lynch EM; Boyken SE; Huang P-S; Stewart L; DiMaio F; Kollman JM; Luisi BF; Matsuura T; Catterall WA; Baker D Computational design of transmembrane pores. Nature 2020, 585, 129–134. [PubMed: 32848250]
22. Latorraca NR; Fastman NM; Venkatakrishnan AJ; Frommer WB; Dror RO; Feng L Mechanism of substrate translocation in an alternating access transporter. Cell 2017, 169, 96–107.e12. [PubMed: 28340354]
23. Lee Y; Nishizawa T; Yamashita K; Ishitani R; Nureki O Structural basis for the facilitative diffusion mechanism by SemiSWEET transporter. Nat. Commun 2015, 6, 6112. [PubMed: 25598322]

24. Kim DE; Chivian D; Baker D Protein structure prediction and analysis using the Robetta server. Nucleic Acids Res. 2004, 32 (Web Server), W526–W531. [PubMed: 15215442]
25. Yang J; Anishchenko I; Park H; Peng Z; Ovchinnikov S; Baker D Improved protein structure prediction using predicted interresidue orientations. Proc. Natl. Acad. Sci. U. S. A 2020, 117, 1496–1503. [PubMed: 31896580]
26. Alford RF; Leaver-Fay A; Jeliazkov JR; O'Meara MJ; DiMaio FP; Park H; Shapovalov MV; Renfrew PD; Mulligan VK; Kappel K; Labonte JW; Pacella MS; Bonneau R; Bradley P; Dunbrack RL; Das R; Baker D; Kuhlman B; Kortemme T; Gray JJ The Rosetta all-atom energy function for macromolecular modeling and design. J. Chem. Theory Comput 2017, 13, 3031–3048. [PubMed: 28430426]
27. Baek M; DiMaio F; Anishchenko I; Dauparas J; Ovchinnikov S; Lee GR; Wang J; Cong Q; Kinch LN; Schaeffer RD; Millán C; Park H; Adams C; Glassman CR; DeGiovanni A; Pereira JH; Rodrigues AV; van Dijk AA; Ebrecht AC; Opperman DJ; Sagmeister T; Buhlheller C; Pavkov-Keller T; Rathinaswamy MK; Dalwadi U; Yip CK; Burke JE; Garcia KC; Grishin NV; Adams PD; Read RJ; Baker D Accurate prediction of protein structures and interactions using a three-track neural network. Science 2021, 373, 871–876. [PubMed: 34282049]
28. Jumper J; Evans R; Pritzel A; Green T; Figurnov M; Ronneberger O; Tunyasuvunakool K; Bates R; Žídek A; Potapenko A; Bridgland A; Meyer C; Kohl SAA; Ballard AJ; Cowie A; Romera-Paredes B; Nikolov S; Jain R; Adler J; Back T; Petersen S; Reiman D; Clancy E; Zielinski M; Steinegger M; Pacholska M; Berghammer T; Bodenstein S; Silver D; Vinyals O; Senior AW; Kavukcuoglu K; Kohli P; Hassabis D Highly accurate protein structure prediction with AlphaFold. Nature 2021, 596, 583–589. [PubMed: 34265844]
29. Pezeshkian W; König M; Wassenaar TA; Marrink SJ Backmapping triangulated surfaces to coarse-grained membrane models. Nat. Commun 2020, 11, 2296. [PubMed: 32385270]
30. Lee J; Cheng X; Swails JM; Yeom MS; Eastman PK; Lemkul JA; Wei S; Buckner J; Jeong JC; Qi Y; Jo S; Pande VS; Case DA; Brooks CL; MacKerell AD; Klauda JB; Im W CHARMM-GUI input generator for NAMD, GROMACS, AMBER, OpenMM, and CHARMM/OpenMM simulations using the CHARMM36 additive force field. J. Chem. Theory Comput 2015, 12, 405–413. [PubMed: 26631602]
31. Wu EL; Cheng X; Jo S; Rui H; Song KC; Dávila-Contreras EM; Qi Y; Lee J; Monje-Galvan V; Venable RM; Klauda JB; Im W CHARMM-GUI membrane builder toward realistic biological membrane simulations. J. Comput. Chem 2014, 35, 1997–2004. [PubMed: 25130509]
32. Jo S; Lim JB; Klauda JB; Im W, CHARMM-GUI membrane builder for mixed bilayers and its application to yeast membranes. Biophys. J 2009, 97, 50–58. [PubMed: 19580743]
33. Jo S; Kim T; Iyer VG; Im W CHARMM-GUI: A web-based graphical user interface for CHARMM. J. Comput. Chem 2008, 29, 1859–1865. [PubMed: 18351591]
34. Huang J; Rauscher S; Nawrocki G; Ran T; Feig M; de Groot BL; Grubmüller H; MacKerell AD CHARMM36m: an improved force field for folded and intrinsically disordered proteins. Nat. Methods 2016, 14, 71–73. [PubMed: 27819658]
35. Klauda JB; Venable RM; Freites JA; O'Connor JW; Tobias DJ; Mondragon-Ramirez C; Vorobyov I; MacKerell AD; Pastor RW Update of the CHARMM all-atom additive force field for lipids: validation on six lipid types. J. Phys. Chem. B 2010, 114, 7830–7843. [PubMed: 20496934]
36. Xu L; Chen LY Identification of a new allosteric binding site for cocaine in dopamine transporter. J. Chem. Inf. Model 2020, 60, 3958–3968. [PubMed: 32649824]
37. Xu L; Chen LY Association of sigma-1 receptor with dopamine transporter attenuates the binding of methamphetamine via distinct helix–helix interactions. Chem. Biol. Drug Des 2021, 97, 1194–1209. [PubMed: 33754484]
38. Berendsen HJC; Postma JPM; van Gunsteren WF; DiNola A; Haak JR Molecular dynamics with coupling to an external bath. J. Chem. Phys 1984, 81, 3684–3690.
39. Darden T; York D; Pedersen L Particle mesh Ewald: An N·log(N) method for Ewald sums in large systems. J. Chem. Phys 1993, 98, 10089–10092.
40. Nosé S A unified formulation of the constant temperature molecular dynamics methods. J. Chem. Phys 1984, 81, 511–519.

41. Hoover WG Canonical dynamics: Equilibrium phase-space distributions. Phys. Rev. A 1985, 31, 1695–1697.
42. Parrinello M; Rahman A Crystal structure and pair potentials: A molecular-dynamics study. Phys. Rev. Lett 1980, 45, 1196–1199.
43. Parrinello M; Rahman A Polymorphic transitions in single crystals: A new molecular dynamics method. J. Appl. Phys 1981, 52, 7182–7190.
44. Berendsen HJC; van der Spoel D; van Drunen R GROMACS: A message-passing parallel molecular dynamics implementation. Comput. Phys. Commun 1995, 91, 43–56.
45. Abraham MJ; Murtola T; Schulz R; Páll S; Smith JC; Hess B; Lindahl E GROMACS: High performance molecular simulations through multi-level parallelism from laptops to supercomputers. SoftwareX 2015, 1–2, 19–25.
46. Kutzner C; Páll S; Fechner M; Esztermann A; Groot BL; Grubmüller H More bang for your buck: Improved use of GPU nodes for GROMACS 2018. J. Comput. Chem 2019, 40, 2418–2431. [PubMed: 31260119]
47. Baker NA; Sept D; Joseph S; Holst MJ; McCammon JA Electrostatics of nanosystems: Application to microtubules and the ribosome. Proc. Natl Acad. Sci. U. S. A 2001, 98, 10037–10041. [PubMed: 11517324]
48. Halestrap AP; Denton RM Specific inhibition of pyruvate transport in rat liver mitochondria and human erythrocytes by α-cyano-4-hydroxycinnamate. Biochem. J 1974, 138, 313–316. [PubMed: 4822737]
49. Halestrap AP The mitochondrial pyruvate carrier. Kinetics and specificity for substrates and inhibitors. Biochem. J 1975, 148, 85–96. [PubMed: 1156402]
50. Trott O; Olson AJ AutoDock Vina: Improving the speed and accuracy of docking with a new scoring function, efficient optimization, and multithreading. J. Comput. Chem 2010, 31, 455–461. [PubMed: 19499576]
51. Vanommeslaeghe K; Hatcher E; Acharya C; Kundu S; Zhong S; Shim J; Darian E; Guvench O; Lopes P; Vorobyov I; Mackerell AD CHARMM general force field: A force field for drug-like molecules compatible with the CHARMM all-atom additive biological force fields. J. Comput. Chem 2010, 31, 671–690. [PubMed: 19575467]
52. Wang J; Cieplak P; Kollman PA How well does a restrained electrostatic potential (RESP) model perform in calculating conformational energies of organic and biological molecules? J. Comput. Chem 2000, 21, 1049–1074.
53. Halestrap AP Pyruvate and ketone-body transport across the mitochondrial membrane. Exchange properties, pH-dependence and mechanism of the carrier. Biochem. J 1978, 172, 377–387. [PubMed: 28726]
54. Porcelli AM; Ghelli A; Zanna C; Pinton P; Rizzuto R; Rugolo M pH difference across the outer mitochondrial membrane measured with a green fluorescent protein mutant. Biochem. Biophys. Res. Commun 2005, 326, 799–804. [PubMed: 15607740]
55. Azarias G; Perreten H; Lengacher S; Poburko D; Demaurex N; Magistretti PJ; Chatton JY Glutamate transport decreases mitochondrial pH and modulates oxidative metabolism in astrocytes. J. Neurosci 2011, 31, 3550–3559. [PubMed: 21389211]
56. Webb B; Sali A Comparative protein structure modeling using MODELLER. Curr. Protoc. Bioinformatics 2016, 54, 5.6.1–5.6.37. [PubMed: 27322406]
57. Nagampalli RSK; Quesñay JEN; Adamoski D; Islam Z; Birch J; Sebinelli HG; Girard RMBM; Ascenção CFR; Fala AM; Pauletti BA; Consonni SR; de Oliveira JF; Silva ACT; Franchini KG; Leme AFP; Silber AM; Ciancaglini P; Moraes I; Dias SMG; Ambrosio ALB Human mitochondrial pyruvate carrier 2 as an autonomous membrane transporter. Sci. Rep 2018, 8, 3510. [PubMed: 29472561]
58. Smart OS; Neduvelil JG; Wang X; Wallace BA; Sansom MSP HOLE: A program for the analysis of the pore dimensions of ion channel structural models. J. Mol. Graph 1996, 14, 354–360. [PubMed: 9195488]
59. Oonthonpan L; Rauckhorst AJ; Gray LR; Boutron AC; Taylor EB Two human patient mitochondrial pyruvate carrier mutations reveal distinct molecular mechanisms of dysfunction. JCI Insight 2019, 5, e126132.

60. Hildyard JCW; Ämmälä C; Dukes ID; Thomson SA; Halestrap AP Identification and characterisation of a new class of highly specific and potent inhibitors of the mitochondrial pyruvate carrier. Biochim. Biophys. Acta 2005, 1707, 221–230. [PubMed: 15863100]

61. Yamashita Y; Vinogradova EV; Zhang X; Suciu RM; Cravatt BF A chemical proteomic probe for the mitochondrial pyruvate carrier complex. Angew. Chem. Int. Engl 2020, 59, 3896–3899.

62. Halestrap AP The mechanism of the inhibition of the mitochondrial pyruvate transportater by α-cyanocinnamate derivatives. Biochem. J 1976, 156, 181–183. [PubMed: 942399]

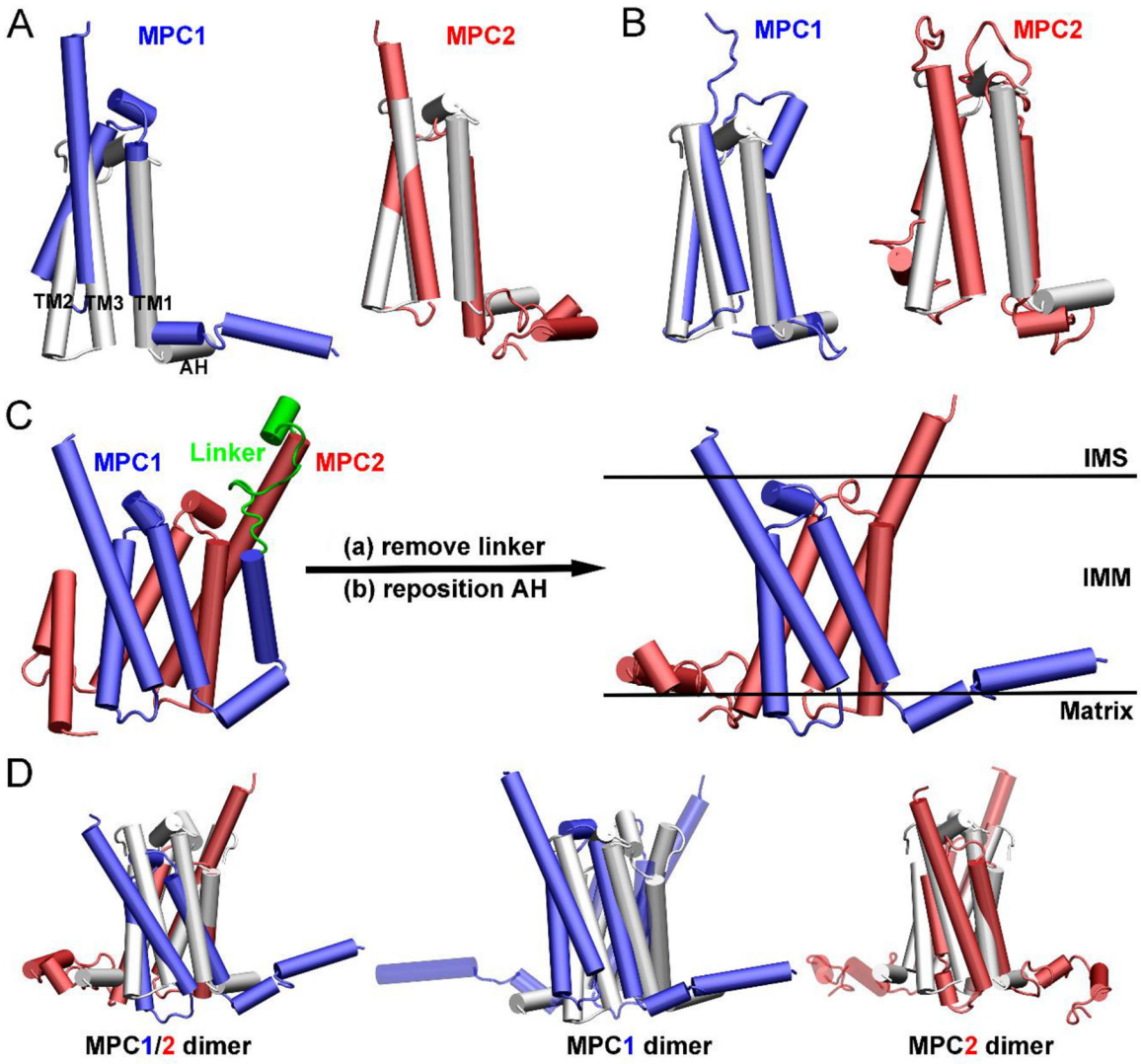

Fig. 1.

(**A**) Superposition of the *de novo* models of MPC1 (blue) and MPC2 (red) with the SemiSWEET protein (light gray). (**B**) Superposition of the homology models of MPC1 (blue) and MPC2 (red) with the SemiSWEET protein (light gray) (PDB ID: 4QND). (**C**) An illustration of the construction of MCP1/2 heterodimer from the *de novo* model of MPC1/2 with a linker containing 20 glycine residues (green). AH denotes the N-terminal amphipathic helix. IMS and IMM denote the intermembrane space and the inner mitochondrial membrane, respectively. (**D**) Superposition of the *de novo* models of MPC1/2 heterodimer, MPC1, and MPC2 homodimers with the dimeric form the SemiSWEET protein (light gray). The SemiSWEET dimer was generated based on the symmetric operations in the PDB file 4QND.

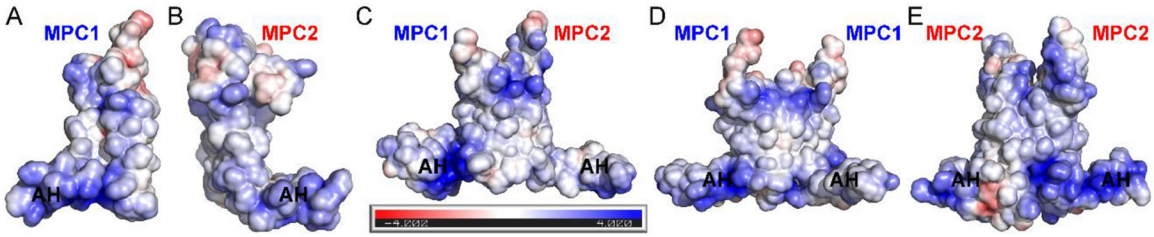

Fig. 2.

Electrostatic potential surface calculated for MPC complexes. The negative potential surface is colored in red whereas the positive potential surface is colored in blue. AH denotes the N-terminal amphipathic helix. (A) MPC1 monomer; (B) MPC2 monomer; (C) MPC1/2 heterodimer; (D) MPC1 homodimer; and (E) MPC2 homodimer.

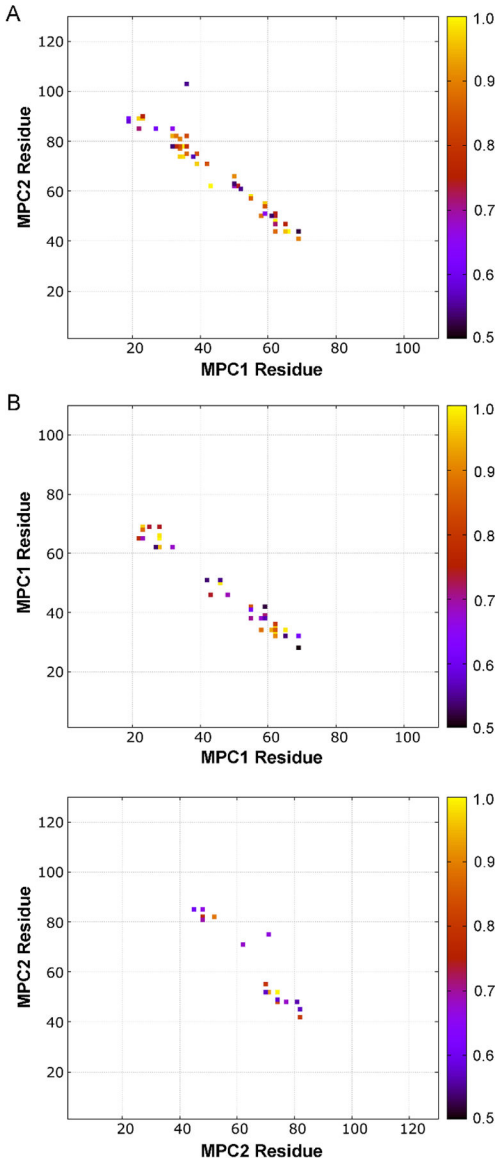

Fig. 3.

Contact maps calculated for human MPC1/2 heterodimer (A), MPC1 homodimer (B), and MPC2 homodimer (C). A contact occurs if any atom in MPC monomer is within 3 Å of any atom in another MPC monomer, and only a contact frequency >0.5 (50%) is shown. Contact frequency was calculated using the last 500-ns trajectory of each simulation. For details of contacting residues, see Tables S4–S6.

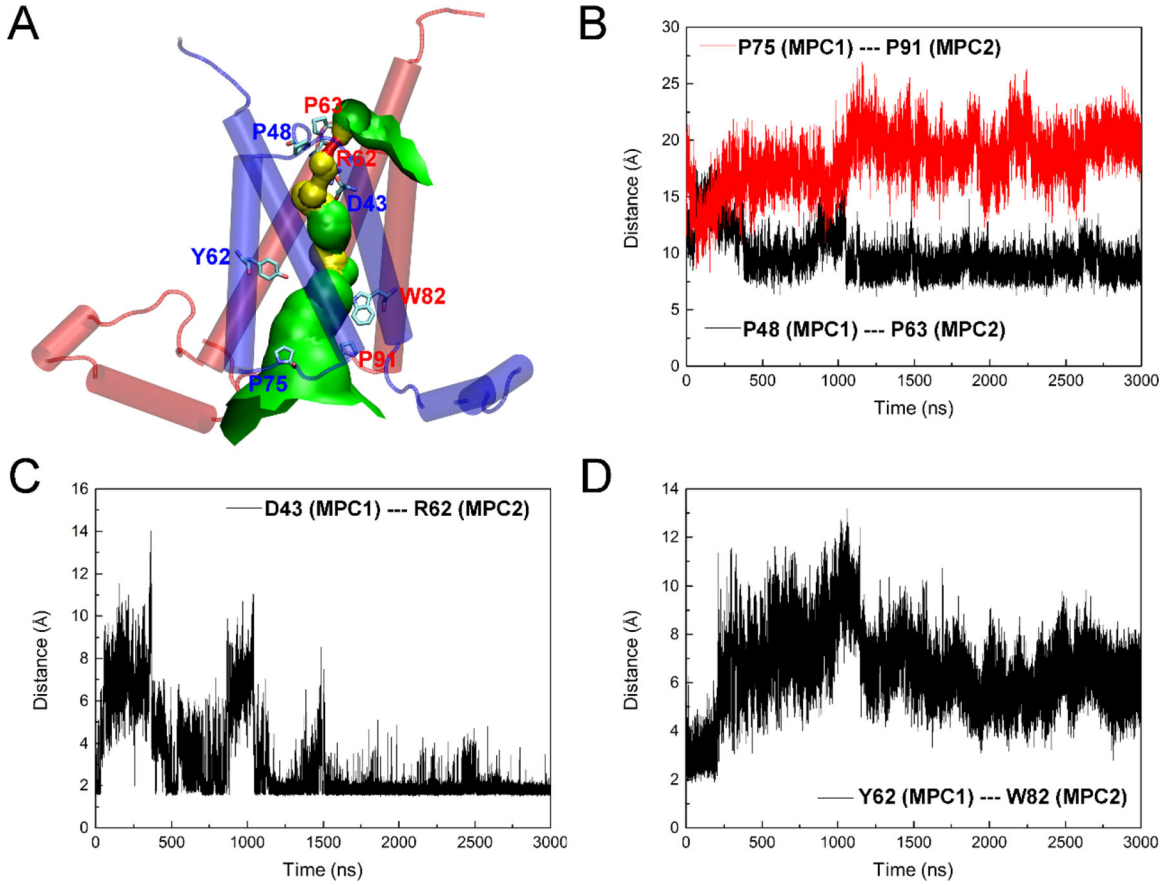

Fig. 4.

(A) Representative conformation of MPC1/2 heterodimer in an inward-open state. MPC1 and relevant residues are colored in blue, and MPC2 and relevant residues are colored in red. (B) The minimal distances between Pro48 of MPC1 and Pro63 of MPC2 and between Pro75 of MPC1 and Pro91 of MPC2 over simulations. (C) The minimal distance between Asp43 of MPC1 and Arg62 of MPC2 over simulations. (D) The minimal distance between gating residues Tyr62 of MPC1 and Trp82 of MPC2.

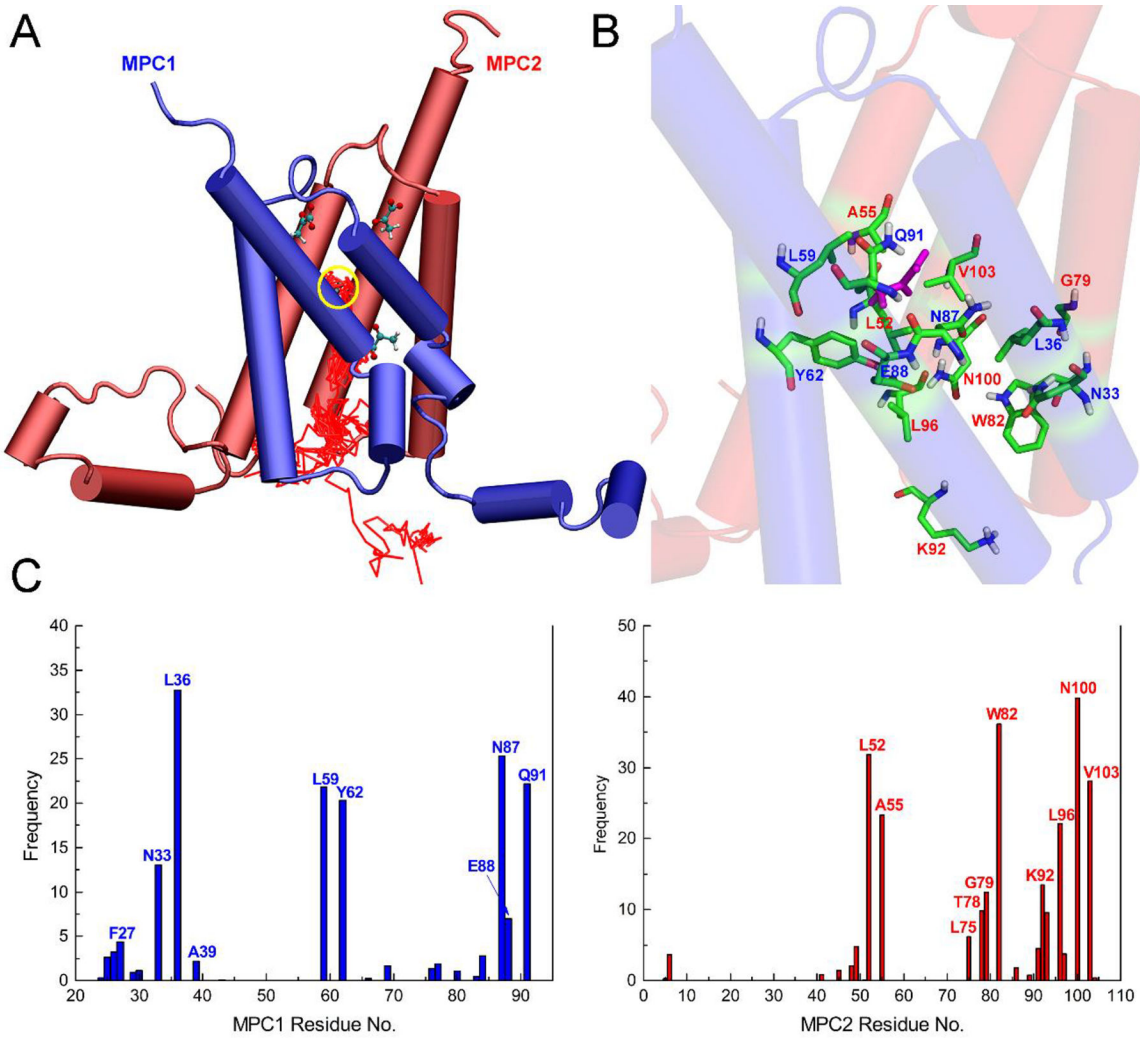

Fig. 5.

Results of MD simulations of MPC1/2 in complex with pyruvates. (A) The initial binding position of pyruvates. The pyruvate whose trace is monitored is circled in yellow. The MPC1/2 is initially in the inward-open conformation. (B) Interacting residues of MPC1 (colored in blue) and MPC2 (colored in red) with the circled pyruvate during translocation. (C and D) The contact frequency of residues of MPC1 (C) and MPC2 (D) with the circled pyruvate during pyruvate transport.

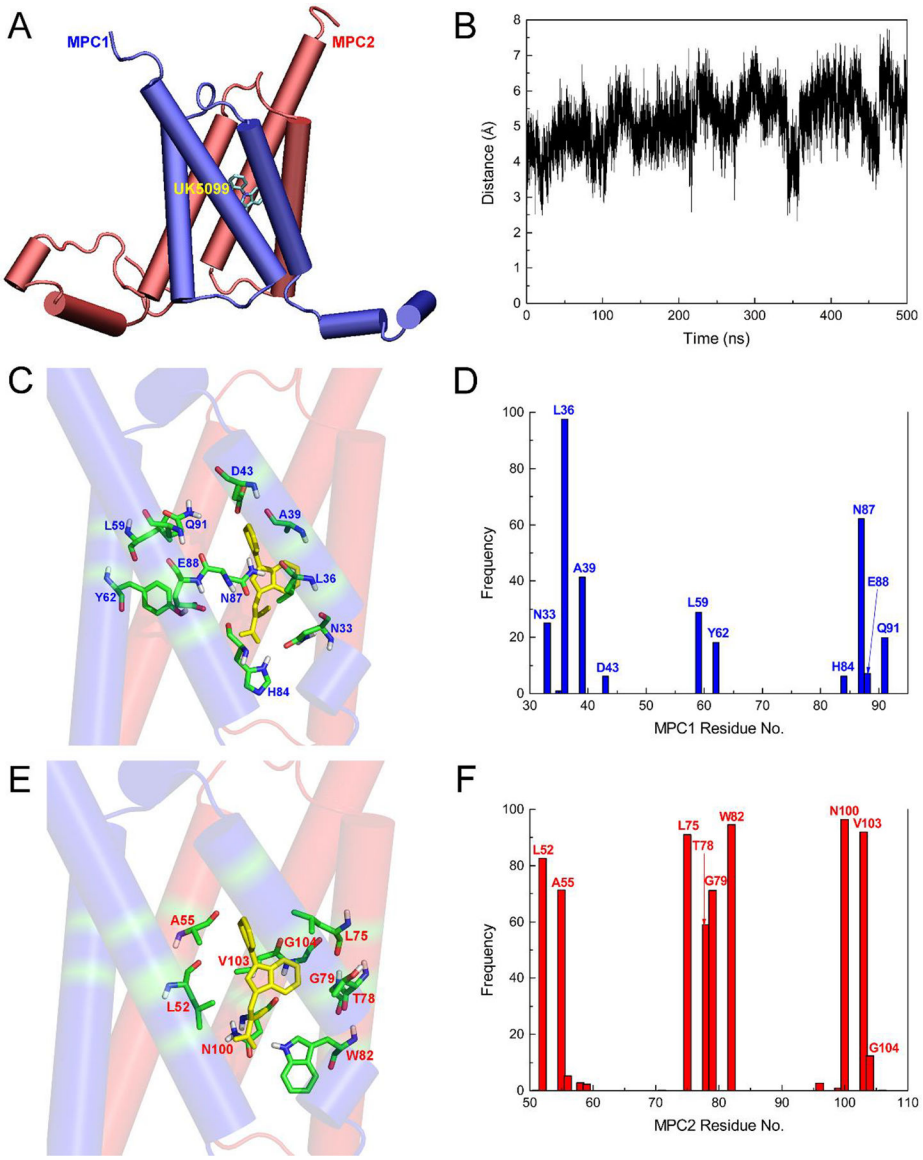

Fig. 6.

Results of MD simulations of MPC1/2 in complex with UK5099. (A) The initial binding site of UK5099 in MPC1/2. (B) The distance between the center-of-mass of MPC1/2 and the center-of-mass of UK5099. (C and D) The interacting residues of MPC1 with UK5099 and corresponding contact frequencies. (E and F) The interacting residues of MPC2 with UK5099 and corresponding contact frequencies.

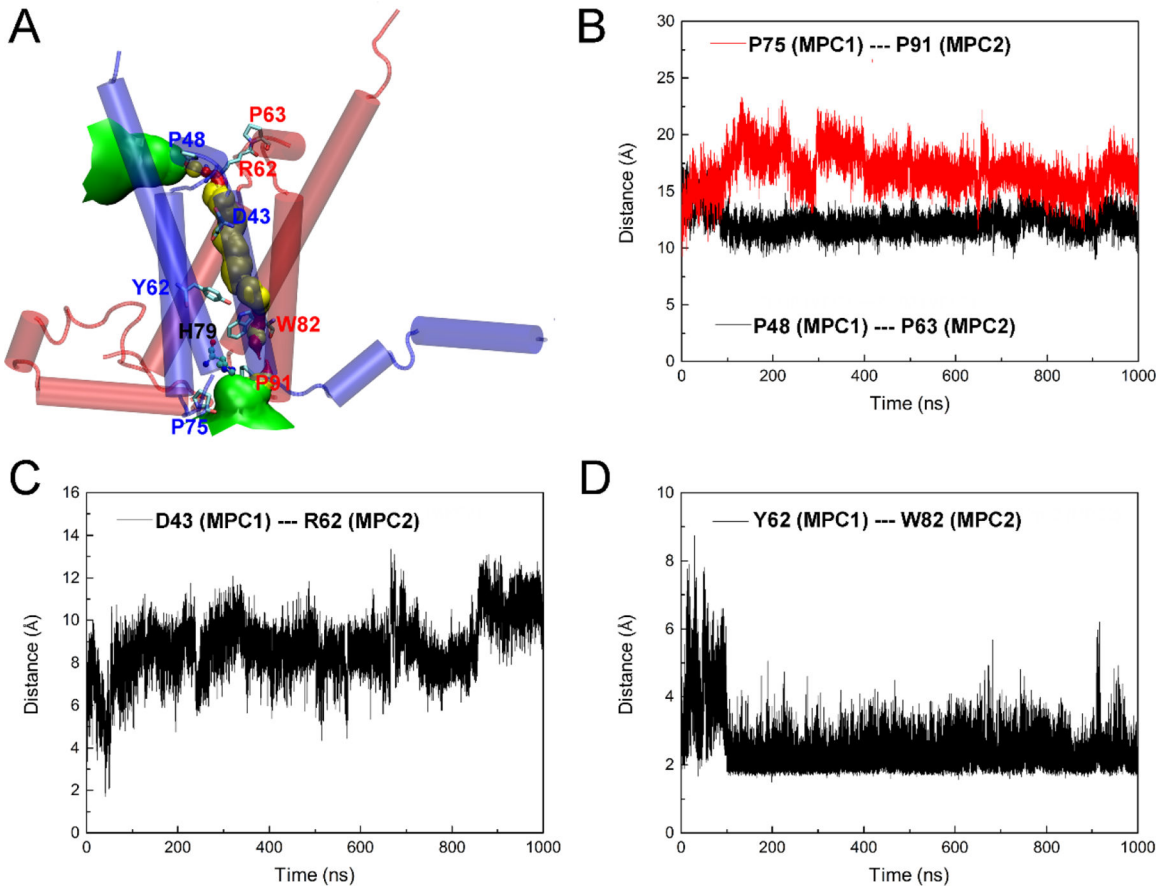

Fig. 7.

(A) Representative conformation of MPC1/2 heterodimer with the MPC1 L79H mutation. The initial conformation is the same outward-open state of MPC1/2 heterodimer as shown in Fig. S4. (B) The minimal distances between Pro48 of MPC1 and Pro63 of MPC2 and between Pro75 of MPC1 and Pro91 of MPC2 over simulations. (C) The minimal distance between Asp43 of MPC1 and Arg62 of MPC2 over simulations. (D) The minimal distance between gating residues Tyr62 of MPC1 and Trp82 of MPC2.